Chemical Engineering Journal 512 (2025) 162700

Contents lists available at ScienceDirect

Chemical Engineering Journal

journal homepage: www.elsevier.com/locate/cej

Intensifying steam methane reforming and water-gas shift in tandem via rapid pulsed Joule heating

Rucha Railkar [a], Yeonsu Kwak [a], Dionisios G. Vlachos [a,b,*]

[a] Department of Chemical and Biomolecular Engineering, University of Delaware, 150 Academy St., Newark, DE 19716, United States
[b] Delaware Energy Institute, 221 Academy St., Newark, DE 19716, United States

ARTICLE INFO

Keywords:
Hydrogen
Steam Methane Reforming
Electrification
Joule Heating
Microkinetic Model
Process Intensification

ABSTRACT

Steam methane reforming (SMR) is the primary industrial method for syngas (a mixture of carbon monoxide (CO) and hydrogen (H_2)) and H_2 production. SMR is one of the most carbon-intensive processes. Due to the ineffectiveness of the water-gas shift (WGS) reaction at the high SMR temperatures, high-purity H_2 requires two downstream WGS reactors. This study demonstrates how dynamic Joule heating can intensify SMR and WGS in a single reactor, boosting H_2 yield. We show that rapid pulsing drives methane conversion and H_2/CO ratios beyond steady-state limits, mostly at higher pressures and steam-rich feeds through thermodynamic analysis, transient kinetic modeling, and experiments. Our simulations highlight the role of pulse shape in maximizing both conversion and H_2/CO ratios leveraging high- and low-temperature regimes. Experimental results confirm that pulsed heating is more efficient than conventional and steady-state heating, maximizing H_2 productivity and reforming rates. These findings position rapid pulsed Joule heating as an intensifying approach to integrate high-temperature endothermic and low-temperature exothermic, equilibrium-limited reactions.

1. Introduction

Hydrogen's unparalleled energy density and versatile applications across fuel cells, transportation, metallurgy, and chemical manufacturing underscore its importance in energy transition [1–3]. Steam methane reforming (SMR) is the cost-effective, commercial thermal hydrogen production method, particularly in regions with abundant natural gas [4,5]. It has a high energy demand ~ 7-10 kWh / kg of H_2 produced [6].

In a typical SMR process, pressured steam and methane are sent through a reformer to produce syngas, which is then processed through two water-gas shift (WGS) reactors to convert CO to CO_2 and H_2 [4]. The overall reactions in the SMR (reaction 1: R1) and the WGS (reaction 2: R2) reactors are

$$CH_4 + H_2O \leftrightarrow CO + 3H_2 \tag{R1}$$

$$CO + H_2O \leftrightarrow CO_2 + H_2 \tag{R2}$$

We summarize key information on the commercial SMR and WGS processes in Table 1. Conventional SMR processes employ nickel (Ni) catalysts, prized for their high activity and economic viability [7]. Despite Ni being the commercial catalyst [8], Ni-based kinetic models remain an active area of research, especially in industrially relevant conditions. The apparent activation energy varies widely (60-360 kJ/mol) due to diverse active sites, supports, and promoters [9–13]. Reduced rate expression models differ in rate-limiting steps at low and high temperatures and dominant surface species [14]. A few micro-kinetic models [15–18] combine some first-principles calculations and the bond order conservation method or experimentally correct energies by fitting specific experiments.

Noble metals, like Pt, Pd, and Rh, have also been explored [19–21]. While Pt and Rh are expensive, they are more active syngas catalysts. Amjad et al. [22] reported 1.5% Rh/CeO_2 as the best-performing catalyst, achieving high activity at ~600 °C, whereas Pt/CeO_2 reached full conversion at 745 °C. Ni-based catalysts are inexpensive and have good activity but typically require higher active material loading (around 12 wt%) than noble metals (1-2%) and have low dispersion. Simulations of catalytic plate reactors and analysis of reaction times demonstrated that Rh is up to 25 times faster than Ni between 900 and 1500 K [23]. These findings highlight that Rh and Pt-based catalysts can be key for modular, intensified SMR reactors for remote and offshore processing to convert natural gas, currently burned or recompressed and injected back into the wells, into platform syngas.

---

* Corresponding author at: Department of Chemical and Biomolecular Engineering, University of Delaware, 150 Academy St., Newark, DE 19716, United States.
E-mail address: vlachos@udel.edu (D.G. Vlachos).

https://doi.org/10.1016/j.cej.2025.162700
Received 26 November 2024; Received in revised form 13 April 2025; Accepted 15 April 2025
Available online 15 April 2025
1385-8947/© 2025 Elsevier B.V. All rights reserved, including those for text and data mining, AI training, and similar technologies.

The endothermic equilibrium-limited nature of SMR ($\Delta H = 206$ kJ/mol) necessitates high temperatures. In contrast, the tandem exothermic WGS ($\Delta H = -41$ kJ/mol) is favored at lower temperatures, and as a result, its contribution at typical SMR reaction conditions is modest. This thermodynamic mismatch, coupled with the risk of Ni or Rh catalyst coking at high temperatures [24], has spurred innovative process intensification strategies. Examples include addressing thermodynamic limitations [25], fluidized bed operation enhancing heat and mass transfer and catalyst-sorbent mixing [26], direct heating instead of inefficient external heating [27], adsorption [28], membrane separation, coupled catalytic reactors to shift equilibrium [29], plasma technology [30], and novel catalysts [31–33], all aimed at enhancing energy efficiency and enabling more compact hydrogen production systems [34].

Electrification technologies, particularly Joule heating [35–38], can improve the efficiency of SMR processes [35,39]. Wismann et al. demonstrated the electrification of the reactor metal tube to enhance heating uniformity and catalyst efficiency [34]. Electrification of SMR (eSMR) can achieve higher energy efficiency and flexibility, with anticipated efficiencies of ≥99% using renewable electricity [40]. Moreover, an eSMR system using Rh/Al_2O_3-coated SiSiC foam achieved near-complete methane conversion above 700°C, with 61% energy efficiency and 2.0 kWh/Nm^3 H_2 specific power consumption, offering strong decarbonization potential [36,41]. eSMR can significantly enhance thermal efficiency and reduce hydrogen production costs compared to conventional methods [42]. Alternative reactor and catalyst designs have also been introduced [43–45].

In our recent works [35,39,46,47], we leverage rapid, dynamic Joule heating to accelerate sluggish kinetics of endothermic, equilibrium-limited reactions. We use a thin carbon fiber tape as the Joule heating element [35,39]. The low thermal mass of the carbon fiber tape and high conductivity enable rapid temperature pulses up to kHz frequencies and a catalyst operating at isothermal conditions [35]. Simple gas-phase prototype models qualitatively explained the experimentally observed rate enhancement, while microkinetics highlighted the effects of rapid pulse heating on the chemistry, surface coverages, and reaction pathways. The pulse-induced enhancement in reaction rate with lower energy use is generic for endothermic reactions. Inspired by early forced periodic operation works [48–50], a fundamental prerequisite is to rapidly pulse the temperature around the steady state at low conversions where enhancements are needed. In process intensification terminology, temperature pulsing intensifies dynamic processes (time-average rate enhancement) by short exposures to high temperatures. Low temperatures, achieved when the power is turned off, do not typically contribute to intensification; they are essential to energy savings.

Here, we extend this strategy to eSMR on Pt catalysts to assess the process intensification of SMR with WGS in the same reactor. We chose the well-established Pt microkinetic model for reliable predictions. Besides, Pt is superior against deactivation than Ni [51], making it ideal for isolating enhancements from pulsing from catalyst effects. By pulsing temperature, we harness high temperatures to enhance the reforming rate and low temperatures to drive forward the equilibrated WGS reaction, collectively shifting the equilibrium toward H_2 production. As a co-benefit, the exothermicity of the WGS reaction reduces the energy load of the SMR. We combine computational insights with experimental validation and reveal mechanistic insights into reaction pathways, rates, and catalyst stability. Unlike prior works that leveraged only high temperatures, we demonstrate that temporal temperature variation can benefit high- and low-temperature parallel/series reactions in the same reactor. It can effectively eliminate the WGS reactor(s) by shifting the equilibrium via temporal rather than spatial segregation. We present equilibrium calculations followed by steady state and dynamic microkinetic calculations, a comparison to experimental data, and finally, a process intensification and pulse optimization analysis under dilute feedstock conditions. To assess the generality of our results, we employ the Langmuir-Hinshelwood rate expressions of Xu and Froment on the Ni catalyst [52] and compare the process intensification of Pt to Ni. We also perform non-dilute feed simulations reminiscent of commercial operation.

2. Results and discussion

Thermodynamic equilibrium calculations reveal the fundamental behavior of coupled SMR and WGS reactions across vital operational parameters (Fig. 1): two pressures (1 and 10 atm) and steam-to-methane ratios (1:1 and 3:1) in He diluent, chosen to probe the interplay between endothermic reforming and exothermic WGS chemistry. Product species distributions at 1 atm (Fig. 1**A**) and 10 atm (Fig. 1**B**) and CH_4 conversion (Fig. 1**A-C**) exhibit strong pressure and feed composition dependence; CH_4 is more reactive at lower pressures and higher steam content, consistent with the endothermic nature and stoichiometry of SMR. Below 1000 K, CO_2 dominates over CO due to the enhanced role of the WGS reaction. The H_2/CO product ratio (Fig. 1**C**) is a proxy of the WGS contribution; at a value of 3, only the SMR is operative (reaction R1), and the WGS (reaction R2) is ineffective. As the ratio increases, the WGS contribution increases. Increasing the pressure and steam content enhances the contribution of the WGS over the SMR to the product distribution, leading to a larger H_2/CO ratio (Fig. 1**C**). As the temperature increases toward the typical reforming temperatures (~1200 K), the ratio reaches an asymptote slightly greater than 3; WGS contributes only modestly. Eliminating the CO from the product stream for H_2 production requires two downstream WGS reactors operating at lower temperatures than the SMR, as explained below, where the WGS is effective.

For the subsequent calculations, we focus on a modest pressure of 10 atm and an H_2O:CH_4 ratio of 3, which closely mimic industrial conditions, unless otherwise noted. Fig. 2 presents steady-state isothermal microkinetic modeling results for SMR. The CH_4 conversion at 10 atm (Fig. 2**A**) is kinetically limited below 1000 K for both feed compositions, transitioning to an equilibrium-controlled regime above 1300 K. Excess steam over the stoichiometric composition enhances CH_4 conversion. CO_2 forms preferentially in the kinetically controlled regime (800-1000 K), indicating dominant WGS activity (Fig. 2**B**). Similar trends occur at 1 atm (**Fig. S1**). CH*, the predominant surface species at lower temperatures, gives its place to empty sites above 1100 K (Fig. 2**C**). Reaction path analysis [56] (Fig. 2**D**) at low CH_4 conversion (~850 K, <10%) reveals the coupling of SMR and WGS pathways. Following sequential CH_4 dehydrogenation, the carbon species undergoes oxidation, leading to formyl formation. The key step in CO formation is $COH + OH \rightarrow CO + H_2O$, followed by CO desorption. The most influential reaction for CO_2 formation is $CO + OH \rightarrow COOH \rightarrow CO_2 + H$, in line with previous studies

Table 1
Industrial steam methane reforming (SMR) and water-gas shift (WGS) process conditions.

Process	Catalyst	Temperature (°C)	Pressure (bar)	Unit Type	Companies
SMR	Nickel oxide	700-1000°C	15-30	Tubular reformer	Air Liquide [53,54], Linde, Air Products, Topsoe [55]
High-Temperature WGS	Fe_2O_3-Cr_2O_3	350-450°C	15-30	Fixed bed	Air Liquide [53,54], Topsoe [55]
Low-Temperature WGS	Cu-Zn-Al	200-250°C	15-30	Fixed bed	Air Liquide [53,54], Topsoe [55]
Pressure Swing Adsorption for H_2 purification	Zeolites, activated carbon		15-30	Adsorption columns	Air Products, Linde

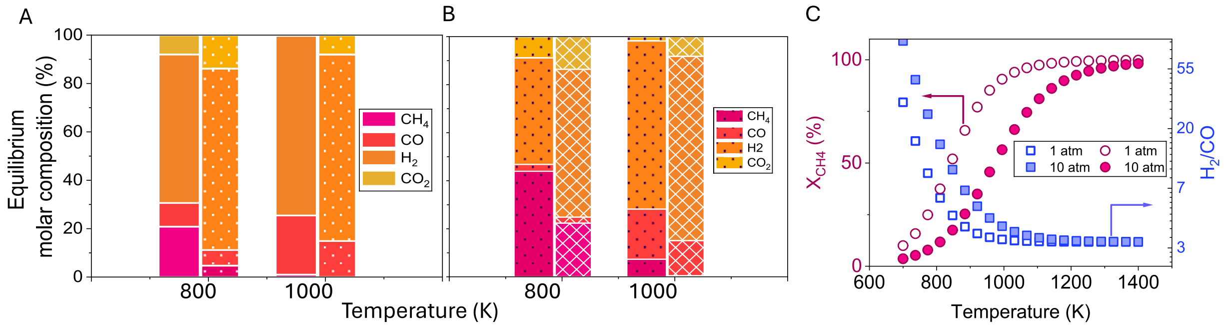

Fig. 1. Thermodynamic equilibrium analysis of SMR. (A) Compositions at 1 atm, H_2O:CH_4 ratios of 5:5 (left bars) and 15:5 (right bars) at 800 K and 1000 K. (B) Corresponding compositions at 10 atm. (C) Temperature dependence of CH_4 conversion (left axis) and H_2:CO ratio (right axis) at 1 atm (open symbols) and 10 atm (filled symbols) with 5% CH_4 and 15% H_2O feed composition. All mixtures are balanced with He.

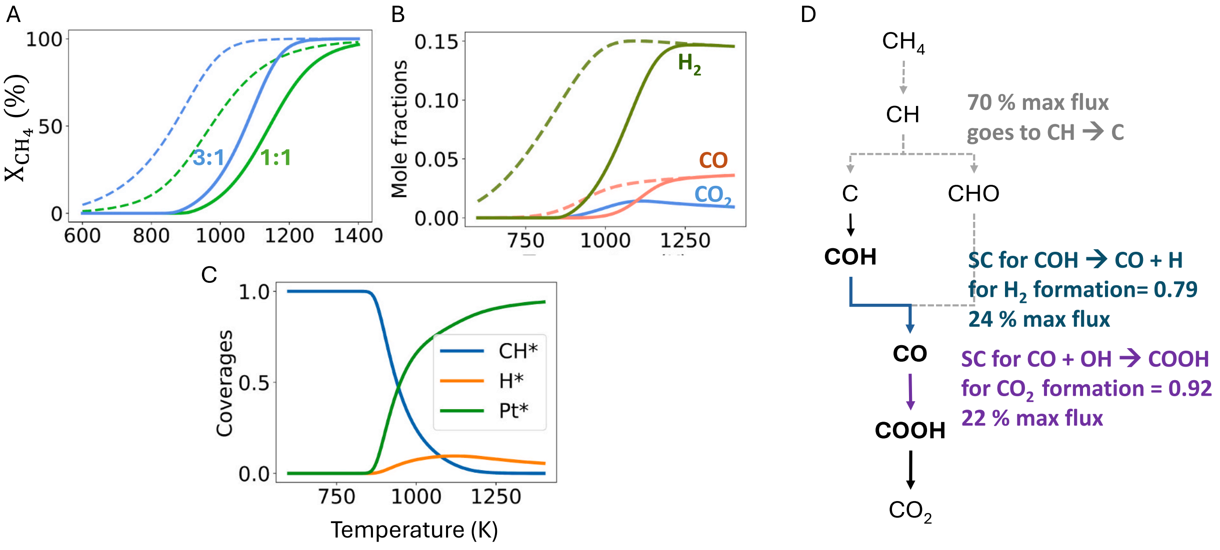

Fig. 2. Isothermal steady-state kinetic modeling analysis of SMR. (A) Steady-state (solid lines) and equilibrium (dashed lines) CH_4 conversion with 5% H_2O (green) and 15% H_2O (blue). (B) Steady state mole fractions of CO (red), CO_2 (blue), and H_2 (green) (solid lines) and equilibrium (dashed lines). (C) Steady state surface coverage of CH* (blue), H* (orange), and Pt* (green). (D) Reaction pathway analysis at 850 K, highlighting key reaction steps (solid lines) and equilibrated pathways (dashed grey lines). The COH+OH→CO+H_2O pathway dominates H_2 formation (sensitivity coefficient: 0.79, blue arrow) while the CO+OH→COOH controls CO_2 formation (sensitivity coefficient: 0.92, purple arrow). All simulations were performed at 10 s residence time, 10 atm, 5% CH_4 feed diluted in He, a weight hourly space velocity (WHSV) of 1.8 kg CH_4/kg Catalyst/h, in a continuous stirred tank reactor. For panels C-D, H_2O:CH_4 = 3:1.

[57]. The competition of these reactions and desorption steps dictates the CO/CO_2 selectivity. **Fig. S2** illustrates the reaction pathway at lower temperatures, highlighting the CH_x dehydrogenation as the highest-flux, non-equilibrated step (and thus rate-determining) consistent with prior work [58] and the high CH* coverages (Fig. 2**C**). The CH_x sequential dehydrogenation equilibrates at higher temperatures, and the influential elementary step shifts further downstream.

Next, we model sinusoidal pulse heating at 1 kHz (Fig. 3). Fig. 3**A** shows the temperature pulse and the corresponding CH_4 conversion and H_2/CO over three periods for one set of conditions to illustrate the dynamics. The CH_4 conversion exhibits a complex profile. It is high at high temperatures, as expected. During the temperature trough, the conversion first drops as the temperature decreases due to the deceleration of the SMR reaction; it then increases before it falls again and finally increases as the temperature rises. This non-monotonic behavior manifests the increased contribution of the WGS reaction R2 at lower temperatures that removes CO from the mixture to make CO_2, promoting thermodynamically the otherwise high-temperature SMR reaction R1. The H_2:CO ratio exhibits a tooth shape; it drops around the peak temperature due to the WGS reaction becoming less effective and rises sharply at the low temperatures of the pulse due to the thriving WGS reaction. The transitions from low to high values are sharp. The H_2:CO rises to $\sim 10^{10}$ at low temperatures, indicating the theoretically predicted ratio when only WGS is active but with an SMR conversion of ~0 (not physically meaningful). Fig. 3**B** shows the phase portrait demonstrating the evolution in the mole fractions as the temperature is pulsed (x-axis). The two lines shown are a closed loop tracing the trajectory that the system follows once a stable periodic state is achieved. The mole fractions of H_2 and CO in Fig. 3**B** rise as the temperature rises from 400 to 1200 K. The rise in CO demands a higher temperature, as expected from the highly endothermic reforming. H_2 increases more than CO from their respective steady-state (previously discussed in Fig. 2**B**) values at T_{avg} of 800 K. This leads to an overall increase in the time average values and an overall boost of the H_2/CO ratio.

Fig. 3**C** shows the evolution of surface coverages during the pulse. While CH* dominates at steady state at lower temperatures and gives rise to vacant sites at elevated temperatures, rapid temperature modulation generates unique surface populations characterized by high H* coverages at low temperatures replaced by vacant sites at high temperatures and vice versa. CH* and C* vary slightly.

Fig. 3**D** shows the distance from equilibrium calculated as $1 - \frac{1}{K_c} \times \frac{y_{CO} \times y_{H_2}}{y_{CH_4} \times y_{H_2O}}$. A value of ~1 indicates a far-from-equilibrium (irreversible) system. Conversely, a value near 0 indicates a near-equilibrium system.

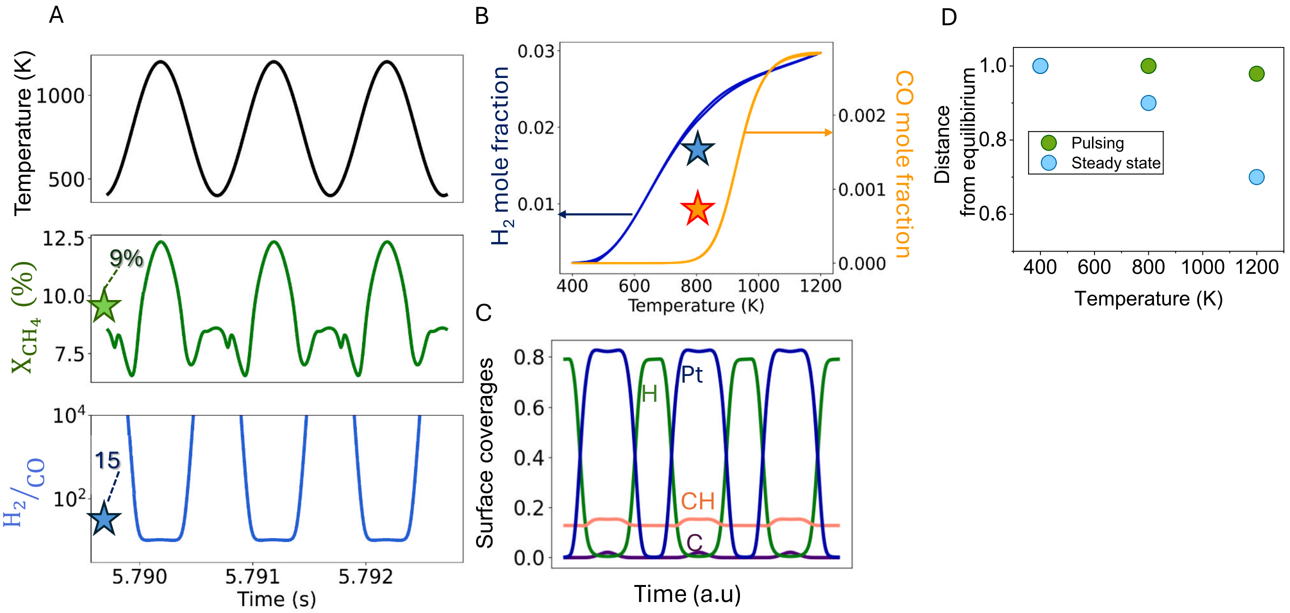

Fig. 3. Dynamic pulse heating results for SMR at 10 atm with 5% CH_4 and 15% H_2O in He. (A) Temperature (top), CH_4 conversion (middle), and H_2:CO ratio (bottom) over three periods. (B) Phase portraits showing instantaneous H_2 (blue on left y-axis) and CO (orange on right y-axis) mole fractions at 800 K. The limit cycles appear as single curves. (C) Pt sites (blue), H (green), C (purple), and CH (salmon) coverages. (D) Approach to equilibrium (normalized: 0 = equilibrium, 1 = furthest from equilibrium) of steady-state (blue) and pulsed (green) operation vs. temperature. Operating conditions: 10 s residence time, WHSV = 1.8 kg CH_4/kg Catalyst/h, 1 kHz pulse frequency, 400 K amplitude in temperature variation around T_{avg} = 800 K. Stars, whenever shown, are time averages.

At steady state (green points), the system remains away from equilibrium at low temperatures but moves closer to equilibrium as the temperature increases. In contrast, pulse heating (blue points) maintains the system further away from equilibrium.

Fig. 4 compares time-averaged pulsing, steady state, and equilibrium data at 1 and 10 atm at two average temperatures T_{avg} of 800 and 1000 K. The temperature in this study lies around or slightly below the industrially relevant temperatures for Ni, with average temperatures between 800 K and 1000 K and a pulse ranging from 500 K to 1300 K. While conventional SMR reactors operate up to 900 °C (∼1200 K) due to reactor wall limitations, electrification enables localized heating of the catalyst bed without high wall temperatures and material constraints. Furthermore, Pt cokes less at high temperatures than Ni, allowing operation at elevated temperatures without significant deactivation.

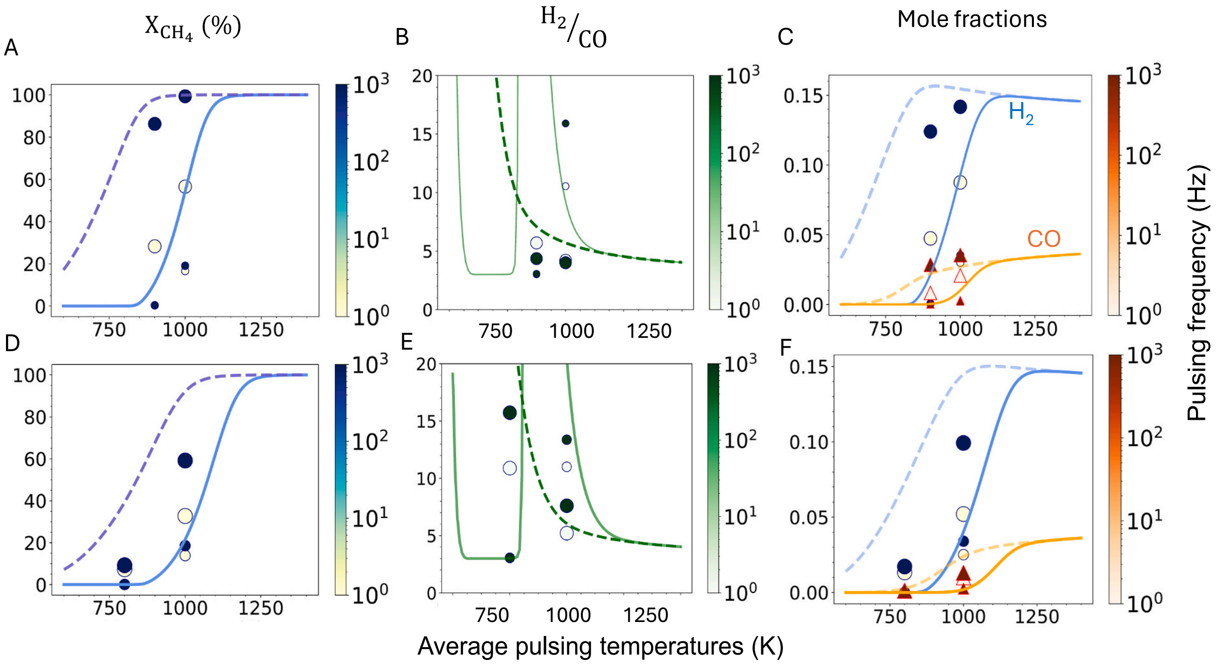

Fig. 4. Analysis of SMR under steady state (solid lines), equilibrium (dashed lines), and pulse heating averages (markers). (A) CH_4 conversion, (B) H_2:CO ratio, and (C) Product mole fractions at 1 atm. (D)-(F) Corresponding data at 10 atm. Operating conditions: pulse amplitudes of 200 K (small markers) and 400 K (large markers), frequencies of 1 (light color) and 1000 Hz (dark color), 10 s residence time, feed composition of 5% CH_4 and 15% H_2O in He, WHSV = 1.8 kg CH_4/kg Catalyst/h. The color bar indicates the frequency (dark markers for 1 kHz; light markers for 1 Hz).

These moderately high average temperatures were also picked allow a large temperature pulsing; but also low, compared to the typical SMR operation, so the conversion improvement from pulsing can be significant. The pulsing frequency and amplitude were parametrically studied instead of optimization via active learning as in prior work [59]. The CH_4 conversion increases with increasing pulsing amplitude (large circles) and frequency (deep blue) over the steady state at both pressures (Fig. 4**A and D**) and approaches equilibrium at the 1 kHz frequency and 400 K amplitude. At 10 atm, pulsing significantly improves reactivity (>3x at $T_{avg} = 1000K$, 1kHz, amplitude = 400 K) but the reaction does not approach equilibrium as closely as at 1 atm. Overall, the conversion/rate enhancement aligns with the expected behavior of endothermic, equilibrium-limited reactions we have reported in prior work for other reactions. Reactivity enhancement is most pronounced at lower T_{avg}, where the steady-state-to-equilibrium gap is the largest and the steady-state conversions are low [46,47] (percent enhancement discussed in supplementary information section S2).

While this study uses a dilute feed, commercial operation uses non-dilute feeds to minimize heating diluents and reduce reactor size. Furthermore, while Pt (or Rh) may be suitable for small-scale applications, Ni-based catalysts will prevail in industrial practice. To assess the impact of pulsing under commercial conditions and the impact of catalyst, we analyzed non-dilute feeds on Pt and Ni-based kinetics [52] (Supplementary Information Section S4). Non-dilute feeds show a greater enhancement in conversion than dilute feeds. This is expected as higher partial pressures of reactants decrease conversion, according to Le Chatelier's principle, making the kinetics slower, where temperature pulsing is more impactful. Similarly to dilution, compared to Pt, the Ni-based model exhibits more sluggish steady state kinetics, and greater enhancement from pulsing. This shows that pulsing over a catalyst with a higher apparent activation barrier could enhance performance more. Consistent with our earlier modeling work on homogeneous kinetics, the overall performance holds across catalysts, but the specifics of the kinetics and catalyst impact the degree of intensification achieved.

Fig. 4**B and E** present the molar H_2/CO ratio for the same conditions. At steady state, the product compositions differ from those at equilibrium under typical conditions. The sharp tooth-shape shows high values at low temperature, low SMR conversion, and hence, low CO mole fractions. At high temperatures, the steady-state ratio approaches the equilibrium value. At low T_{avg} (800–900 K), the thermodynamic limit for the H_2/CO ratio is high. Pulsing within 400–1200 K predominantly operates under WGS-dominated conditions, with some contribution from the low-conversion SMR regime. High-frequency, high-amplitude pulsing enhances the H_2/CO ratio by driving enough reforming to produce CO, subsequently triggering the WGS reaction. This generates more H_2 than CO, moving the ratio closer to its thermodynamic limit.

At higher T_{avg} (1000 K), pulsing (e.g., 600 –1400 K for high amplitude) shifts toward SMR-dominated temperatures. Larger amplitudes at these conditions favor CO formation, reducing the H_2/CO ratio. In contrast, smaller amplitudes (800 – 1200 K) primarily enhance H_2 production, maintaining a higher ratio. This ratio surpasses the corresponding equilibrium H_2/CO ratio at that T_{avg}. This temperature- and amplitude-dependent behavior indicates that higher amplitudes at high T_{avg} drive the system away from the WGS-dominated regime and deeper into SMR conditions, favoring CO over H_2. Regardless of T_{avg} or amplitude, high frequencies consistently benefit both the conversion and the H_2/CO ratio by enhancing overall reaction rates. Among the explored conditions, pulsing at 10 atm, $T_{avg} = 1000$ K, frequency = 1 kHz, and amplitude = 400 K achieved the most pronounced improvement, maximizing conversion while maintaining a favorable H_2/CO ratio.

Figs. 4**C and F** present the H_2 and CO mole fractions. At lower T_{avg}, the H_2 mole fraction (blue circles) significantly exceeds the steady-state predictions (blue lines), increasing by over 100x, while the CO mole fraction (warm-colored triangles) shows a smaller increase. At higher T_{avg} and amplitudes, the CO mole fraction rises more than H_2. This behavior indicates a pressure-enhanced interplay between SMR and WGS pathways under dynamic conditions.

These observations reveal that pulsing at low T_{avg} increases conversion and the H_2/CO ratio below the thermodynamic limit. In contrast, pulsing at high T_{avg} with large amplitudes enhances conversion but lowers the H_2/CO ratio due to increased CO production; lower amplitudes at high T_{avg} can surpass the equilibrium H_2/CO. A balanced approach—pulsing with moderate amplitude and high frequency at a moderately high T_{avg}—can optimize both conversion and the H_2/CO ratio, surpassing steady-state limits.

Overall, SMR at 10 atm offers a more extensive regime of T_{avg} and amplitude to improve performance. This study highlights, for the first time, that low temperatures during pulsing promote equilibrated exothermic reactions in the kinetically limited regime of an endothermic equilibrium-limited reaction, complementing the established benefits of high-temperature endothermic reactions.

Fig. 5**A** shows experimental data for the methane conversion vs. temperature for three operating heating modes. RPH reaches higher conversions at lower temperatures than CJH, consistent with this system's predicted pulse-induced rate enhancement (Fig. 4**)** and the experimentally observed enhanced rate for other reactions [35,39]. CJH achieves a similar conversion with conventional heating (CH), which heats the entire reactor and the gases outside the reactor. Fig. 5**B** reveals that RPH achieves high H_2 production rates at significantly reduced power consumption than the CH and even the CJH due to the localized heating and the power being off for long parts of each cycle. Specifically, the RPH reaches maximum productivity with less than 1/3 of the power of the CH. The energy savings are a major advantage of RPH. We discuss the efficiency of both heating methods in the experimental methods sections and Supplementary Information (section S6).

The model validation against experiments (Fig. 5**C and D**) reveals varying degrees of agreement. The model captures the general trend for CJH and RPH and, importantly the rate enhancement (Fig. 5**C**). The model and experiment agree better for RPH and closely follow the equilibrium curve. The CJH model predictions are offset from the experimental data by about ~100 K, but the curves have a similar shape. Overall, the agreement is decent, given that the experimental reactor has complex flow patterns and transport[37], which are absent from a simple CSTR reactor. Such phenomena are amplified during pulsing, where the hot zone next to the tape oscillates, causing a variable residence time not captured by the model. Fig. 5**D** shows the H_2/CO ratio at the same pulsing conditions, with both heating methods giving a value of 3–4 at high temperatures, closely approaching equilibrium at higher temperatures. The model and experimental data indicate that pulsing under these conditions offers almost no improvement over the steady state. Due to the practical limitations of the current experimental setup, below we optimize the pulse parameters further and exploit unexplored regions computationally only.

To understand the impact of dynamic operation on process intensification, we modeled a reference case of three reactors operating in series at steady state. This system mimics the industrial H_2 production [54,55] (summarized in Table 1). We consider a high- and a low-temperature WGS reactor downstream of the SMR reactor to convert CO to CO_2 and produce nearly pure H_2. In the model, the output from each reactor becomes the input for the next one. The model captures spatial temperature variation across the three reactors operated sequentially. We simulate this three-reactor system using our microkinetic model at steady state and eventually compare it with the temporally sinusoidal single-pulsing reactor in Fig. 6. The residence times and operating conditions are listed in the figure caption. While exact residence times of the commercial processes vary and catalysts differ from the one used here, the residence time of the low-temperature WGS is longer than the high-temperature WGS reactor to allow nearly complete conversion of CO.

For the three reactors in series, the SMR reactor achieves a 77% CH_4 conversion (near equilibrium); no further reforming occurs in the

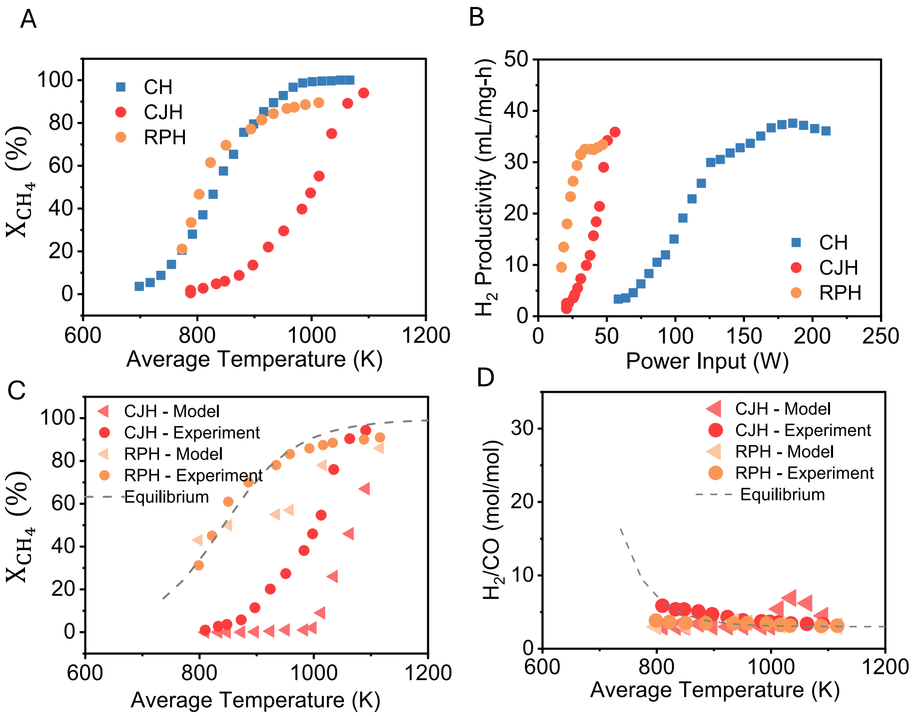

Fig. 5. Conventional heating (CH) in a furnace, continuous Joule heating (CJH) at steady state, and rapid pulse heating (RPH) for SMR. (A) Experimental CH_4 conversion vs. temperature and (B) H_2 productivity vs. applied power. Model comparison against experimental data for (C) CH_4 conversion and (D) H_2/CO molar ratio vs. steady state or average temperature for CJH and RPH. Experimental conditions: 10 mg of 5 wt% Pt/Al_2O_3 catalyst loaded on 38x8x0.21 mm^3 CFP, 1.5% CH_4, 3% H_2O in He, CJH in steady state operation; RPH at 1 Hz frequency (alternating with 20% duty cycle). Modeling conditions: 1.5% CH_4 and 3% H_2O in He, WHSV = 1.8 kg CH_4/kg Catalyst/h, conditions that mimic our experiments.

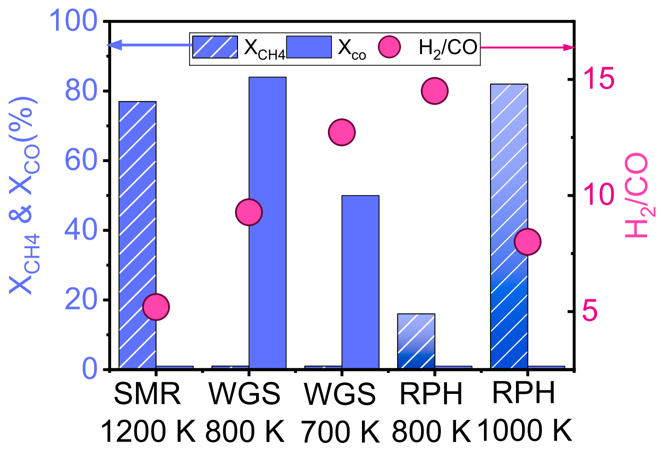

Fig. 6. Spatial vs. temporal performance of two reaction systems. CH_4 conversion (hashed blue bars) and CO conversion (solid blue bars) on the left y-axis and H_2/CO in pink circles on the right y-axis at 10 atm. The three left datasets refer to reactors in series operating at the indicated temperatures with residence times of 1 s, 10 s, and 100 s, respectively. The last two datasets refer to pulsing with T_{avg} indicated, frequency 1 kHz, amplitude 400 K, and a 10 s residence time. The feed to each SMR reactor (first, fourth, and fifth datasets) is 5% CH_4 and 15% H_2O in He. WHSV for the first = 12.6, second = 0.97, third = 0.1, and fourth and fifth datasets = 1.8 kg CH_4/kg Catalyst/h.

subsequent WGS reactors due to low operating temperatures. The CO conversion in the SMR reactor is low due to the thermodynamic limitations of the WGS reaction. The first WGS reactor operating at 800 K achieves an 82% CO conversion, due to high kinetic activity and more steam, compared to the second WGS reactor, which achieves only a 47% conversion. At the exit of this 3-step process, we reach >99% CO conversion and 77% CH_4 conversion. The H_2/CO ratio increases from 5 (SMR) to 8 (first WGS reactor) to ~12 (second WGS reactor); 5 is the thermodynamically achievable ratio in the reforming reaction with a 3:1 feed. The H_2/CO ratio at the exit of the second WGS reactor corresponds to a low percent CO due to a significant fraction of CO_2 and unreacted CH_4 and H_2O in the product stream.

Next, we turn to the dynamic operation of a single SMR reactor. The rightmost two datasets in Fig. 6 correspond to pulsing at the listed operating conditions. At T_{avg} of ~800 K, the methane conversion is low, ~18%, and the H_2/CO is 15. This T_{avg} is comparable to the first WGS reactor but much lower than the SMR reactor operating at steady state at 1200 K. The conversion is 10x of the steady state at 800 K but much lower than the steady state SMR reactor at 1200 K; H_2/CO is higher than the 3-step process. Pulsing significantly enhances performance, but this low conversion is not practical. The rightmost dataset at T_{avg} of 900 K achieves a conversion close to equilibrium and higher than the steady state of the SMR of 1200 K and an H_2/CO of 8, which is 2x that of the steady state and close to the exit of the first WGS reactor. The dynamic SMR reactor performs comparably to the two steady-state reactors (SMR and first WGS). The residence time of the single dynamic SMR reactor is significantly lower than the steady state three-reactor system and slightly lower than the combined SMR and first WGS reactor.

Figs. 4–6 show that pulse frequency and amplitude critically influence H_2/CO and conversion, with the time spent at high and low temperatures impacting SMR and WGS chemistries. We further explore pulse shapes to optimize both H_2/CO and CH_4 conversion.

The results demonstrate sinusoidal pulsing enhances performance, but its symmetric nature restricts the heating and cooling rates and achievable temperatures within each cycle, capping both the highest and lowest temperatures. Recognizing the importance of spending more time at lower temperatures to promote the WGS, following a brief high-temperature reforming phase, we explore an asymmetric pulse shape using a linear ramp-up and a linear cool-down schedule (Fig. 7**A**). In practice, the heat phase is closer to linear, and the cooling phase to an

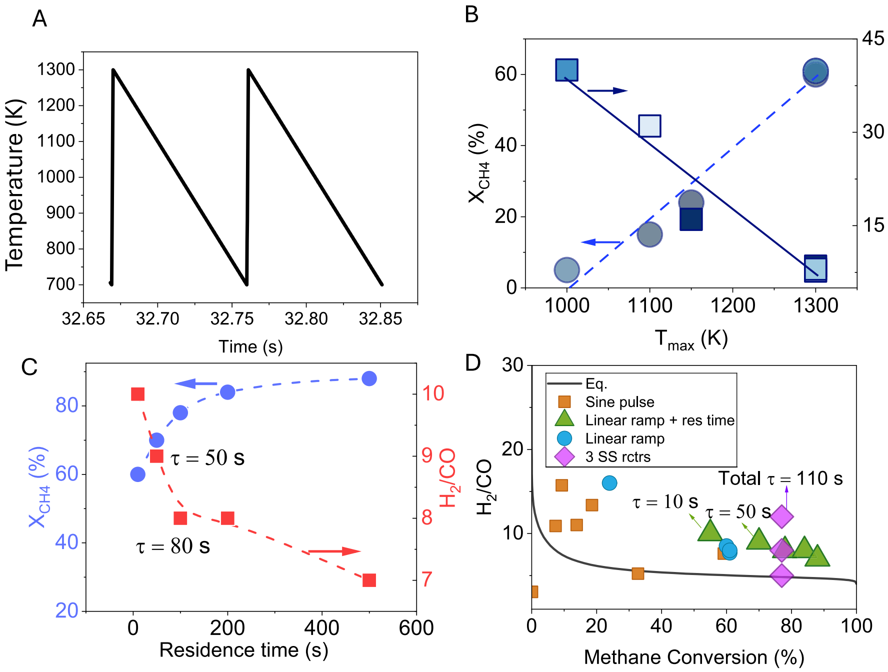

Fig. 7. Impact of pulse parameters and process conditions on SMR performance. (A) Sample temperature pulse for 1 ms heating and 0.9 s cooling time, maximum temperature of 1300 K, and starting temperature of 700 K. (B) CH_4 conversion (left axis, circles) and H_2:CO ratio (right axis, squares) vs. pulse maximum temperature for different heating/cooling rates (color-coded, details in **Table S1**). (C) Effect of residence time (10-500 s) on conversion and H_2:CO ratio at fixed heating time (1 ms) and cooling time (0.9 s). Operating conditions for (A) and (B): 10 atm pressure, 5% CH_4, 15% H_2O in He. (D) Performance map showing H_2:CO ratio vs. CH_4 conversion comparing equilibrium prediction (grey line obtained by varying temperature) with different operating modes: sinusoidal pulsing (orange squares), varied heating/cooling times (blue circles), varied residence times (green triangles), and three-reactor steady-state process (pink diamonds). All pulsing conditions at 10 atm with 5% CH_4 and 15% H_2O in He.

exponential decay. This approach allows us to investigate varying slopes and pulse widths around a T_{avg}. The minimum and maximum temperatures and the heating and cooling times (or slopes) are taken as independent variables defining a tooth-shaped pulse. Fig. 4 and Fig. 5 show that pulsing at an average temperature of ~900 – 1000 K at 10 atm and 3:1 H_2O:CH_4 gives a near-equilibrium, high CH_4 conversion and an H_2/CO ratio of about 8. Hence, we first use a T_{avg} of ~900 K at a fixed residence time (10 s) to optimize the pulse (Fig. 7**B**). In Fig. 7**B**, Bayesian optimization via NEXTorch [60] explores the effects of the four variables on the conversion and H_2/CO ratio. We discuss details of the optimization algorithm in Supplementary Information section S5. The data in **Table S1** along with a correlation analysis [61] (**Fig. S4**) show that the heating and cooling rates are far less significant than the pulse maximum temperature. This is evident in Fig. 7**B**, where the markers for various heating and cooling times overlap, and a clear correlation vs. the maximum pulse temperature is seen. The higher the maximum temperature of a pulse, the higher the conversion and the lower the H_2/CO, establishing a clear tradeoff between conversion and H_2/CO.

Fig. 7**C** examines the role of residence time, with the heating time fixed at 1 ms and the cooling time at 0.9 s. Increasing the residence time enhances conversion but decreases the H_2/CO ratio. A residence time of ~50–80 s, still less than the cumulative residence time of the three-step process, achieves $X_{CH4} = 78\%$ with a H_2/CO ratio of 8-9. These findings suggest that a single pulse-heated reactor could effectively replace an SMR and a WGS reactor, intensifying the process. We summarize all data in Fig. 7**D** and compare them to equilibrium and spatial varying steady-state temperature data of the three-reaction system. The gray curve represents the equilibrium limit, while the pink diamonds (three reactors) show the benchmark performance for traditional setups. A sinusoidal pulse (orange squares) enhances the H_2/CO ratio but achieves this at only <50% conversion. This highlights a limitation in achieving simultaneous enhancement in both metrics. In contrast, rapid heating with prolonged cooling (blue markers) achieves higher conversions. Finally, tweaking the residence time matches the performance of 1 SMR and 1 WGS reactor. Specifically, a dynamically operated SMR with a residence time of 10 s ($1/10^{th}$ of the 3-step process) can replace two reactors with slightly lower conversion but a slightly higher H_2/CO ratio. For a residence time of 50 s (1/2 of the 3-step process), the performance is directly comparable to that of two reactors. Overall, the optimization demonstrates that the capital costs associated with using two reactors (one SMR and one WGS), including controllers, connections, peripherals, and the need for two catalysts (with a WGS catalyst like Pt being typically more expensive than the Ni-based catalyst of the SMR), could be reduced by transitioning to a single pulse-heated electrified reactor. The reduction in reactor size by two orders of magnitude significantly reduces the reactor/catalyst cost, and Pt or Rh-based catalysts can be relevant to future distributed manufacturing.

3. Conclusions

This study provides insights into dynamic eSMR operation using temperature pulsing. It simulates the process with a full microkinetic model, provides experimental evidence in support of the simulations, and employs active learning to optimize the pulse. It explores the concept of whether short, high temperature exposures of the SMR chemistry can enhance the rate over the steady state whereas the temperature reduction of the pulse can drag the WGS chemistry along its equilibrium line by shifting CO to CO_2 and enhancing H_2 production. By doing so, one could combine the spatially segregated SMR and WGS reactors into a single unit via temporal temperature variation. Dynamic operation may also harness the energy released during WGS to support the SMR reaction at high temperatures, improving overall energy efficiency.

We found that dynamic pulse heating enhances CH_4 conversion and improves H_2/CO ratios under optimized conditions. Computational and experimental results highlight that this performance enhancement is most pronounced at lower average temperatures, higher steam-to-carbon ratios, and elevated pressures. The effectiveness of pulsing depends on the interplay between pulse parameters (e.g., heating and cooling durations) and reactor parameters (e.g., residence time). Short heating durations, prolonged cooling times, and residence times exceeding those of a single reformer enable a single RPH SMR reactor to achieve performance comparable to two reactors in series (SMR and the first WGS) with lower power consumption, highlighting significant process intensification. While we focused primarily on diluted feeds, our computations indicate that non dilute streams should exhibit enhanced performance gains from pulsing. Importantly, the concept holds across catalysts and could be applied to the commercial Ni-based catalysts; catalysts more sluggish than Pt could exhibit larger enhancements than Pt. This approach offers a more compact, efficient, and sustainable solution for hydrogen production, advancing electrification efforts in the chemical industry. RPH emerges as an energy-efficient approach, achieving higher H_2 productivity at lower power input than the CH and CJH, with a comparable H_2/CO ratio. The consistent product selectivity across heating methods underscores that the underlying SMR and WGS chemistry remains unchanged.

4. Methods

4.1. Modeling

4.1.1. Microkinetic model, reactor model, and analysis

A previously published first-principles microkinetic model [62] was converted into OpenMKM format [63]. OpenMKM allows temperature pulsing, has state-of-the-art solvers in C++, and executes quickly. The model includes elementary reactions on Pt(111) surface and is thermodynamically consistent. CFD simulations [37] and experiments [35,39,59] indicate that a small volume near the carbon fiber tape remains isothermal. We use this volume in our calculations. The reactor has significant flow recirculation under typical conditions that leads to back-mixing, mimicking a CSTR. We use an ideal gas reactor model where pressure follows temperature pulses while conserving total mass [46]. This approach prevents negative mass flow rates from reverse flows during pulsing. The Cantera reactor routine calculates volumetric flow rate changes, while mass flow rate variations result only from adsorption and desorption at the catalyst surface, not from flow in or out. While industrial reactors for SMR are typically tubular, we have chosen a CSTR model to more easily determine the effect of rapid temperature pulsing and better mimic the experimental Joule-heated reactor setup that has significant back mixing. Our model applies to modular reactors like monoliths and foams, where minimal temperature gradients ensure uniform heating. The approach can also be applied to a plug flow reactor (PFR), modeled as a series of a sufficient number of CSTRs or as a partial differential equation model. Scaling up fixed-bed reactors will also require spatially resolved models. In such an approach, the reactor could be divided into a series of differential control volumes or segments, each governed by coupled mass and energy balances. These balances account for convective flow, species transport, reaction kinetics, and heat exchange. An exciting prospect is the ability to tune the pulsed heating temporally and spatially. Recent advances in electrified spatiotemporal heating [64–66] enable zoned temperature modulation to maintain kinetically favorable conditions along the reactor length. CFD [37,67,68] coupled with kinetic modeling [68,69] will be needed to guide scalable designs, though challenges persist in heat management, pressure tolerance, and renewable energy integration at industrial scales [70]. We expect enhancement at high temperatures still away from equilibrium, with colder reactor regions of spatially inhomogeneous reactors showing less improvement. Solid-gas temperature gradients could be favorable for catalytic chemistry over gas-phase reactions.

The results were analyzed using reaction path analysis (RPA) using OpenMKM's reaction flux outputs and the partial equilibrium index (PEI), a metric for the distance from equilibrium. The PEI is defined as PEI=$r_f/(r_f+r_b)$, where $r_{f,b}$ are the forward (f) and backward (b) rates of elementary reactions. When PEI>0.5, the reaction happens in the forward direction. To get a sense, PEIs of 0.55, 0.6, 0.7, 0.8, and 0.9 imply r_f/r_b of 1.2, 1.5, 2.3, 4, and 9. Conversely, when PEI<0.5, the reaction happens in reverse. PEI of 0.45, 0.4, 0.3, 0.2., and 0.1 imply r_f/r_b of 0.8, 0.7, 0.4, 0.25, and 0.1. Values 0.45<PEI<0.55 indicate rates within 20% of each other and that the elementary reaction is practically equilibrated. The normalized sensitivity factor (SF) of the rate of production of N_2 with respect to the i^{th} elementary reaction is defined as $SF_{ki} = \frac{d\ln y_k}{d\ln p_i}$, where p_i is the parameter perturbed (the forward rate constant and implicitly the reverse rate constant due to keeping the equilibrium constant fixed); y_k is the production rate (of H_2).

4.2. Reactivity tests

The steam methane reforming reactions were performed in a custom-designed Joule heating (JH) reactor. The reactor's core consisted of a 58 x 8 mm carbon fiber paper (CFP) substrate (Freudenberg H23, Freudenberg Performance Materials GmbH & Co. KG) having 38 x 8 mm exposed area, which was used either in its uncoated form or impregnated with about 10.0 mg of 5 wt% Pt/Al_2O_3 catalyst (sourced from Sigma Aldrich, USA). A gas mixture comprising 100 mL/min total CH_4 + He was directed downward through the reactor, controlled by precise mass flow controllers. For experiments involving steam, the incoming gas mixture was bubbled through water, resulting in the introduction of approximately 3% water vapor into the gas stream. To analyze the hydrocarbon products in real-time, the reactor's outlet was connected to a micro gas chromatograph (Agilent 990 MicroGC).

4.3. Experimental heating efficiency of conventional and joule heating methods

We quantified the effectiveness of both heating methods through systematic measurements of energy input and hydrogen production. For conventional heating, we monitored electrical power consumption using calibrated power meters connected to the furnace, while thermocouples tracked temperature distribution across the catalyst bed. For rapid pulse heating (RPH), we measured instantaneous power delivery using calibrated voltage and current meters to determine total electrical power input. We additionally employed infrared thermography to validate temperature distributions and heating patterns. To evaluate heating effectiveness, we calculated the energy efficiency ratio by dividing the hydrogen space-time yield ($g_{H2}/g_{cat}\cdot h$) by the total electrical power input (W), providing a time-averaged measure of energy utilization. This metric quantifies how efficiently each method converts electrical energy into products. Our analysis demonstrated that RPH achieves substantially higher effectiveness than conventional heating, attributable to its direct energy delivery to the catalyst surface and the off periods.

CRediT authorship contribution statement

Rucha Railkar: Writing – review & editing, Writing – original draft, Investigation, Formal analysis. **Yeonsu Kwak:** Writing – original draft, Formal analysis. **Dionisios G. Vlachos:** Writing – review & editing, Supervision, Project administration, Funding acquisition, Formal analysis.

Declaration of competing interest

The authors declare that they have no known competing financial interests or personal relationships that could have appeared to influence the work reported in this paper.

Acknowledgments

This work was supported by the Department of Energy grant number DE-SC0025378.

Appendix A. Supplementary data

Supplementary data to this article can be found online at https://doi.org/10.1016/j.cej.2025.162700.

Data availability

Data will be made available on request.

References

[1] J.D. Holladay, J. Hu, D.L. King, Y. Wang, An overview of hydrogen production technologies, Catal. Today 139 (4) (2009) 244–260, https://doi.org/10.1016/j.cattod.2008.08.039.

[2] P. Nikolaidis, A. Poullikkas, A comparative overview of hydrogen production processes, Renew. Sustain. Energy Rev. 67 (2017) 597–611, https://doi.org/10.1016/j.rser.2016.09.044.

[3] IEA, The Future of Hydrogen, 2019.

[4] A.O. Oni, K. Anaya, T. Giwa, G. Di Lullo, A. Kumar, Comparative assessment of blue hydrogen from steam methane reforming, autothermal reforming, and natural gas decomposition technologies for natural gas-producing regions, Energy Conversion and Management 254 (2022) 115245, https://doi.org/10.1016/j.enconman.2022.115245.

[5] H.F. Sheet, Hydrogen production–steam methane reforming (SMR), New York State Energy Res. Dev. Authority New York (2005).

[6] How much CO2 is produced from steam methane reforming?, Hydrogen Newsletter (2023).

[7] C.L. Basel, Steam methane reforming, Clariant Ltd.

[8] L. Joshi, Steam-Methane-Reforming, 2023. https://www.greenh2world.com/post/steam-methane-reforming.

[9] How much CO2 is produced from steam methane reforming?, Hydrogen Newsletter (2023).

[10] M. Soliman, A. Adris, A. Al-Ubaid, S. El-Nashaie, Intrinsic kinetics of nickel/calcium aluminate catalyst for methane steam reforming, J. Chem. Technol. Biotechnol. 55 (2) (1992) 131–138.

[11] J. Wei, E. Iglesia, Isotopic and kinetic assessment of the mechanism of reactions of CH4 with CO2 or H2O to form synthesis gas and carbon on nickel catalysts, J. Catal. 224 (2) (2004) 370–383.

[12] N. Bodrov, L. Apel'baum, M. Temkin, Kinetics of the reaction of methane with water vapour catalysed by nickel on a porous carrier, Kinetika L Kataliz 8 (1967) 821–828.

[13] J. Wei, C. Georgakis, Chemical Reaction Engineering—Boston, ACS Publications1982.

[14] P. Van Beurden, On the catalytic aspects of steam-methane reforming, Energy Research Centre of the Netherlands (ECN), technical report I-04-003 (2004).

[15] L. Aparicio, Transient isotopic studies and microkinetic modeling of methane reforming over nickel catalysts, J. Catal. 165 (2) (1997) 262–274.

[16] D.W. Blaylock, Y.-A. Zhu, W.H. Green, Computational investigation of the thermochemistry and kinetics of steam methane reforming over a multi-faceted nickel catalyst, Top. Catal. 54 (2011) 828–844.

[17] H.S. Bengaard, J.K. Nørskov, J. Sehested, B. Clausen, L. Nielsen, A. Molenbroek, J. Rostrup-Nielsen, Steam reforming and graphite formation on Ni catalysts, J. Catal. 209 (2) (2002) 365–384.

[18] K.H. Delgado, L. Maier, S. Tischer, A. Zellner, H. Stotz, O. Deutschmann, Surface Reaction Kinetics of Steam- and CO2-Reforming as Well as Oxidation of Methane over Nickel-Based Catalysts, Catalysts 5 (2) (2015) 871–904.

[19] T. Zhu, P.W. van Grootel, I.A.W. Filot, S.-G. Sun, R.A. van Santen, E.J.M. Hensen, Microkinetics of steam methane reforming on platinum and rhodium metal surfaces, J. Catal. 297 (2013) 227–235, https://doi.org/10.1016/j.jcat.2012.10.010.

[20] G.V.a.A.B.a.G.G.a.E.T. Matteo Maestri and Dionisios, Steam and dry reforming of methane on Rh: Microkinetic analysis and hierarchy of kinetic models, Journal of Catalysis 259(2) (2008) 211-222. 10.1016/j.jcat.2008.08.008.

[21] A.B. Mhadeshwar, D.G. Vlachos, A Catalytic Reaction Mechanism for Methane Partial Oxidation at Short Contact Times, Reforming, and Combustion, and for Oxygenate Decomposition and Oxidation on Platinum, Ind. Eng. Chem. Res. 46 (16) (2007) 5310–5324, https://doi.org/10.1021/ie070322c.

[22] U.-E.-S. Amjad, A. Vita, C. Galletti, L. Pino, S. Specchia, Comparative Study on Steam and Oxidative Steam Reforming of Methane with Noble Metal Catalysts, Ind. Eng. Chem. Res. 52 (44) (2013) 15428–15436, https://doi.org/10.1021/ie400679h.

[23] G.D. Stefanidis, D.G. Vlachos, Intensification of steam reforming of natural gas: Choosing combustible fuel and reforming catalyst, Chem. Eng. Sci. 65 (1) (2010) 398–404, https://doi.org/10.1016/j.ces.2009.06.007.

[24] D.L. Trimm, Coke formation and minimisation during steam reforming reactions, Catal. Today 37 (3) (1997) 233–238.

[25] M. Soliman, S. El-Nashaie, A. Al-Ubaid, A. Adris, Simulation of steam reformers for methane, Tenth international symposium on chemical reaction engineering, Elsevier, 1988, pp. 1801-1806.

[26] K. Johnsen, Sorption-enhanced steam methane reforming in fluidized bed reactors, (2006).

[27] S.A.a.S.J. Bhat, Process intensification aspects for steam methane reforming: An overview, AIChE Journal 55(2) (2009) 408-422. 10.1002/aic.11687.

[28] J.R. Hufton, S. Mayorga, S. Sircar, Sorption-enhanced reaction process for hydrogen production, AIChE J 45 (2) (1999) 248–256.

[29] M. Koga, T. Watanabe, Plate type reformer, Google Patents (1991).

[30] I. Rusu, J.-M. Cormier, On a possible mechanism of the methane steam reforming in a gliding arc reactor, Chem. Eng. J. 91 (1) (2003) 23–31.

[31] J.P. Van Hook, Methane-steam reforming, Catalysis Reviews—Science and Engineering 21(1) (1980) 1-51.

[32] C. Schnell, Reaction mechanism of steam re-forming, J. Chem. Soc. B (1970) 158–163.

[33] P. Münster, H. Grabke, Kinetics of the steam reforming of methane with iron, nickel, and iron-nickel alloys as catalysts, J. Catal. 72 (2) (1981) 279–287.

[34] S.T. Wismann, J.S. Engbæk, S.B. Vendelbo, F.B. Bendixen, W.L. Eriksen, K. Aasberg-Petersen, C. Frandsen, I. Chorkendorff, P.M. Mortensen, Electrified methane reforming: A compact approach to greener industrial hydrogen production, Science 364 (6442) (2019) 756–759, https://doi.org/10.1126/science.aaw8775.

[35] K. Yu, C. Wang, W. Zheng, D.G. Vlachos, Dynamic Electrification of Dry Reforming of Methane with In Situ Catalyst Regeneration, ACS Energy Lett. 8 (2) (2023) 1050–1057, https://doi.org/10.1021/acsenergylett.2c02666.

[36] L. Zheng, M. Ambrosetti, F. Zaio, A. Beretta, G. Groppi, E. Tronconi, Direct electrification of Rh/Al2O3 washcoated SiSiC foams for methane steam reforming: An experimental and modelling study, Int. J. Hydrogen Energy 48 (39) (2023) 14681–14696, https://doi.org/10.1016/j.ijhydene.2022.12.346.

[37] A. Mittal, M. Ierapetritou, D.G. Vlachos, Computational insights into steady-state and dynamic Joule-heated reactors, React. Chem. Eng. (2024), https://doi.org/10.1039/D4RE00114A.

[38] D.S. Mallapragada, Y. Dvorkin, M.A. Modestino, D.V. Esposito, W.A. Smith, B.-M. Hodge, M.P. Harold, V.M. Donnelly, A. Nuz, C. Bloomquist, K. Baker, L. C. Grabow, Y. Yan, N.N. Rajput, R.L. Hartman, E.J. Biddinger, E.S. Aydil, A. D. Taylor, Decarbonization of the chemical industry through electrification: Barriers and opportunities, Joule 7 (1) (2023) 23–41, https://doi.org/10.1016/j.joule.2022.12.008.

[39] K. Yu, S. Sourav, W. Zheng, D.G. Vlachos, Dynamic electrification steers the selectivity of CO2 hydrogenation, Chem. Eng. J. 481 (2024) 148528, https://doi.org/10.1016/j.cej.2024.148528.

[40] T.N. From, B. Partoon, M. Rautenbach, M. Østberg, A. Bentien, K. Aasberg-Petersen, P.M. Mortensen, Electrified steam methane reforming of biogas for sustainable syngas manufacturing and next-generation of plant design: A pilot plant study, Chem. Eng. J. 479 (2024) 147205, https://doi.org/10.1016/j.cej.2023.147205.

[41] L. Zheng, M. Ambrosetti, D. Marangoni, A. Beretta, G. Groppi, E. Tronconi, Electrified methane steam reforming on a washcoated SiSiC foam for low-carbon hydrogen production, AIChE J 69 (1) (2023) e17620, https://doi.org/10.1002/aic.17620.

[42] H. Song, Y. Liu, H. Bian, M. Shen, X. Lin, Energy, environment, and economic analyses on a novel hydrogen production method by electrified steam methane reforming with renewable energy accommodation, Energ. Conver. Manage. 258 (2022) 115513, https://doi.org/10.1016/j.enconman.2022.115513.

[43] J.-F. Peloquin, D. Francoeur, W. Leclerc, D. Mehanovic, J.-F. Dufault, P. Camus, I. J. Castellanos-Beltran, N. Braidy, L.G. Fréchette, M. Picard, Electrified steam methane reforming microreactor, Int. J. Hydrogen Energy 49 (2024) 907–915, https://doi.org/10.1016/j.ijhydene.2023.07.343.

[44] J. Ma, B. Jiang, Y. Gao, K. Yu, Z. Lv, W. Si-ma, D. Yuan, D. Tang, A compact and high-efficiency electrified reactor for hydrogen production by methane steam reforming, Int. J. Hydrogen Energy 47 (98) (2022) 41421–41431, https://doi.org/10.1016/j.ijhydene.2022.04.281.

[45] J. Ma, B. Jiang, L. Li, K. Yu, Q. Zhang, Z. Lv, D. Tang, A high temperature tubular reactor with hybrid concentrated solar and electric heat supply for steam methane reforming, Chem. Eng. J. 428 (2022) 132073, https://doi.org/10.1016/j.cej.2021.132073.

[46] R. Railkar, D. Vlachos, Enhanced Performance of Dynamic Temperature Pulsing: Modeling Insights from Simple Reaction Networks, Ind. Eng. Chem. Res. 63 (1) (2024) 130–138, https://doi.org/10.1021/acs.iecr.3c03198.

[47] R. Railkar, D.G. Vlachos, Microkinetic insights into temperature pulsing for accelerating ammonia decomposition, Int. J. Hydrogen Energy 89 (2024) 583–589, https://doi.org/10.1016/j.ijhydene.2024.09.329.

[48] J. Stolte, L. Özkan, P.C. Thüne, J.W. Niemantsverdriet, A.C.P.M. Backx, Pulsed activation in heterogeneous catalysis, Appl. Therm. Eng. 57 (1) (2013) 180–187, https://doi.org/10.1016/j.applthermaleng.2012.06.035.

[49] J.E. Bailey, Periodic Operation of Chemical Reactors: A review, Chem. Eng. Commun. 1 (3) (1974) 111–124, https://doi.org/10.1080/00986447408960421.

[50] D. Sinčić, J.E. Bailey, Pat-hological dynamic behavior of forced periodic chemical processes, Chem. Eng. Sci. 32 (3) (1977) 281–286, https://doi.org/10.1016/0009-2509(77)80206-6.

[51] M.E. Agnelli, E.N. Ponzi, A.A. Yeramian, Catalytic deactivation on methane steam reforming catalysts. 2. Kinetic study, Industrial & Engineering Chemistry Research 26 (8) (1987) 1707–1713, https://doi.org/10.1021/ie00068a038.

[52] J. Xu, G.F. Froment, Methane steam reforming, methanation and water-gas shift: I. Intrinsic kinetics, AIChE Journal 35 (1) (1989) 88–96, https://doi.org/10.1002/aic.690350109.

[53] Steam Methane Reforming (SMR): Full Steam Ahead by Hydrocarbon Engineering | Air Liquide Engineering & Construction, (2019).

[54] Hydrogen: Forging the future with SMR-X™ technology | Air Liquide.

[55] Convection reformer HTCR | Products | Equipment | Topsoe.

[56] U. Gupta, D.G. Vlachos, Reaction Network Viewer (ReNView): An open-source framework for reaction path visualization of chemical reaction systems, SoftwareX 11 (2020) 100442, https://doi.org/10.1016/j.softx.2020.100442.

[57] A.B.a.V.D.G. Mhadeshwar, Microkinetic Modeling for Water-Promoted CO Oxidation, Water−Gas Shift, and Preferential Oxidation of CO on Pt, The Journal of Physical Chemistry B 108(39) (2004) 15246-15258. https://doi.org/10.1021/jp048698g.

[58] S.S.a.J.K.a.M.P.A.a.J.R.a.F.A.-P.a.T.B.a.S.H. Glenn Jones and Jon Geest Jakobsen and Signe, First principles calculations and experimental insight into methane steam reforming over transition metal catalysts, Journal of Catalysis 259(1) (2008) 147-160. 10.1016/j.jcat.2008.08.003.

[59] Q. Dong, Y. Yao, S. Cheng, K. Alexopoulos, J. Gao, S. Srinivas, Y. Wang, Y. Pei, C. Zheng, A.H. Brozena, H. Zhao, X. Wang, H.E. Toraman, B. Yang, I.G. Kevrekidis, Y. Ju, D.G. Vlachos, D. Liu, L. Hu, Programmable heating and quenching for efficient thermochemical synthesis, Nature 605 (7910) (2022) 470–476, https://doi.org/10.1038/s41586-022-04568-6.

[60] Y. Wang, T.-Y. Chen, D.G. Vlachos, NEXTorch: A Design and Bayesian Optimization Toolkit for Chemical Sciences and Engineering, J. Chem. Inf. Model. 61 (11) (2021) 5312–5319, https://doi.org/10.1021/acs.jcim.1c00637.

[61] pandas.DataFrame.corr — pandas 2.2.3 documentation.

[62] X. Zong, D.G. Vlachos, Reconciling experimental catalytic data stemming from structure sensitivity, Chem. Sci. 14 (16) (2023) 4337–4345, https://doi.org/10.1039/D2SC06819B.

[63] B. Medasani, S. Kasiraju, D.G. Vlachos, OpenMKM: An Open-Source C++ Multiscale Modeling Simulator for Homogeneous and Heterogeneous Catalytic Reactions, Journal of Chemical Information and Modeling 63 (11) (2023) 3377–3391, https://doi.org/10.1021/acs.jcim.3c00088.

[64] Q. Dong, A.D. Lele, X. Zhao, S. Li, S. Cheng, Y. Wang, M. Cui, M. Guo, A. H. Brozena, Y. Lin, T. Li, L. Xu, A. Qi, I.G. Kevrekidis, J. Mei, X. Pan, D. Liu, Y. Ju, L. Hu, Depolymerization of plastics by means of electrified spatiotemporal heating, Nature 616 (7957) (2023) 488–494, https://doi.org/10.1038/s41586-023-05845-8.

[65] X. Wang, X. Qin, W. Zhou, Z. Xu, C. Yu, J. Chang, Joule Heating: A Versatile and Sustainable Heating Strategy with Diverse Applications in Materials Science and Waste Management, J. Mater. Chem. A (2025).

[66] D. Zheng, Q. Xie, F. Li, W. Huang, Z. Qi, J. Dong, G. Li, F. Zhang, Spatiotemporal dynamic temperature variation dominated by ion behaviors during groundwater remediation using direct current, Environ. Pollut. 351 (2024) 124091, https://doi.org/10.1016/j.envpol.2024.124091.

[67] N. Ben Khedher, Z. Ullah, M. Alturki, C.R. Mirza, S.M. Eldin, Effect of Joule heating and MHD on periodical analysis of current density and amplitude of heat transfer of electrically conducting fluid along thermally magnetized cylinder, Ain Shams Eng. J. 15 (2) (2024) 102374, https://doi.org/10.1016/j.asej.2023.102374.

[68] R. Varun Kumar, M. Gopinath M, B. Kusum Kumar, H. Goyal, Machine Learning Model for CFD Simulations of Fluidized Bed Reactors, Industrial & Engineering Chemistry Research 64(2) (2025) 999-1010. https://doi.org/10.1021/acs.iecr.4c02885.

[69] D. Micale, R. Uglietti, M. Bracconi, M. Maestri, Coupling Euler–Euler and Microkinetic Modeling for the Simulation of Fluidized Bed Reactors: an Application to the Oxidative Coupling of Methane, Ind. Eng. Chem. Res. 60 (18) (2021) 6687–6697, https://doi.org/10.1021/acs.iecr.0c05845.

[70] A. Griffin, M. Robertson, Z. Gunter, A. Coronado, Y. Xiang, Z. Qiang, Design and Application of Joule Heating Processes for Decarbonized Chemical and Advanced Material Synthesis, Ind. Eng. Chem. Res. 63 (45) (2024) 19398–19417, https://doi.org/10.1021/acs.iecr.4c02460.